

See discussions, stats, and author profiles for this publication at: <https://www.researchgate.net/publication/282582192>

Core/Shell Face-Centered Tetragonal FePd/Pd Nanoparticles as an Efficient Non-Pt Catalyst for the Oxygen Reduction Reaction

ARTICLE in ACS NANO · OCTOBER 2015

Impact Factor: 12.88 · DOI: 10.1021/acsnano.5b04361

READS

63

9 AUTHORS, INCLUDING:



Guangming Jiang

Zhejiang University

22 PUBLICATIONS 256 CITATIONS

SEE PROFILE



Huiyuan Zhu

Brown University

19 PUBLICATIONS 363 CITATIONS

SEE PROFILE



Gang Lu

California State University, Northridge

108 PUBLICATIONS 1,486 CITATIONS

SEE PROFILE



Zhongbiao Wu

Zhejiang University

147 PUBLICATIONS 4,024 CITATIONS

SEE PROFILE

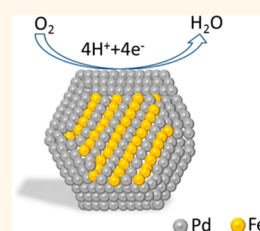
Core/Shell Face-Centered Tetragonal FePd/Pd Nanoparticles as an Efficient Non-Pt Catalyst for the Oxygen Reduction Reaction

Guangming Jiang,^{†,*} Huiyuan Zhu,^{*,†,||} Xu Zhang,[§] Bo Shen,[†] Liheng Wu,[†] Sen Zhang,[†] Gang Lu,[§] Zhongbiao Wu,^{*,†} and Shouheng Sun^{*,†}

[†]Department of Chemistry, Brown University, Providence, Rhode Island 02912, United States, [‡]Department of Environmental Engineering, Zhejiang University, Hangzhou, Zhejiang 310058, China, and [§]Department of Physics and Astronomy, California State University Northridge, Northridge, California 91330, United States.

^{||} Present address: Chemical Sciences Division, Oak Ridge National Laboratory, Oak Ridge, TN 37831, United States.

ABSTRACT We report the synthesis of core/shell face-centered tetragonal (fct)-FePd/Pd nanoparticles (NPs) *via* reductive annealing of core/shell Pd/Fe₃O₄ NPs followed by temperature-controlled Fe etching in acetic acid. Among three different kinds of core/shell FePd/Pd NPs studied (FePd core at ~8 nm and Pd shell at 0.27, 0.65, or 0.81 nm), the fct-FePd/Pd-0.65 NPs are the most efficient catalyst for the oxygen reduction reaction (ORR) in 0.1 M HClO₄ with Pt-like activity and durability. This enhanced ORR catalysis arises from the desired Pt lattice compression in the 0.65 nm Pd shell induced by the fct-FePd core. Our study offers a general approach to enhance Pd catalysis in acid for ORR.



KEYWORDS: FePd · face-centered tetragonal structure · core/shell nanoparticles · electrocatalysis · oxygen reduction reaction

Nanostructured palladium (Pd), especially Pd nanoparticles (NPs), has been a popular choice of catalysts for many chemical reactions.^{1,2} Pd NPs have also been explored as a promising non-Pt catalyst for electrochemical oxidation of formic acid with high CO tolerance^{3–5} and for electrochemical reduction of oxygen^{6–8} with activity in acid superior to carbon-based^{9,10} and metal/metal oxide catalysts.^{11,12} Recent studies indicate that, like Pt, Pd can alloy with a first-row transition metal M (M = Cu, Ni, Co, Fe, *etc.*), and Pd catalytic properties for both fuel oxidation¹³ and oxygen reduction reaction (ORR)^{14–16} can be improved. Especially, when a thin layer of Pd is coated around MPd NP, the Pd–O binding strength is optimized to the level where the Pd catalysis for ORR may become comparable to Pt.^{17,18} Despite the progress made in developing Pd as an alternative catalyst for electrochemical reactions, the Pd-based catalysts demonstrated thus far have poorer durability than Pt in acid,^{16,19–21} and consequently, they are much inferior to Pt in catalyzing ORR.

One new strategy to stabilize the alloy catalyst in the corrosive electrochemical reaction environment, such as in ORR, is to have the alloy adopt an intermetallic structure.²² Take FePt NPs for example, once prepared, these NPs often have a face-centered cubic (fcc)-type solid solution structure, which is unstable (subject to fast Fe leaching) in acid, making it difficult to assess Fe effect on FePt catalysis for ORR in 0.1 M HClO₄. However, when the Fe/Pt atomic ratio is near 50/50, the fcc-FePt can be converted to an intermetallic face-centered tetragonal (fct) structure.²³ Such an fct-structure is formed due to the strong 3d–5d interaction between Fe and Pt along the crystallographic *c*-direction. In this structure, Fe is greatly stabilized, and fct-FePt NPs have shown much enhanced chemical stability against acid etching and therefore much enhanced ORR catalysis.²⁴ The enhanced catalytic efficiency arises from the core/shell fct-FePt/Pt structure in which the Pt lattice in the thin Pt shell (<1 nm) is more compressed than that in the common surface Pt shell from the pure Pt NPs.²⁴ Once the fct-ordering is further

* Address correspondence to
zhuh@ornl.gov,
zbwu@zju.edu.cn,
ssun@brown.edu.

Received for review July 14, 2015
and accepted October 2, 2015.

Published online
10.1021/acs.nano.5b04361

© XXXX American Chemical Society

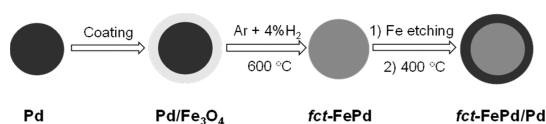


Figure 1. Schematic illustration of the synthesis of core/shell fct-FePd/Pd NPs.

improved, the Pt catalysis in the fct-FePt/Pt NPs can be optimized not only for ORR in 0.1 M HClO₄ but also for hydrogen evolution reaction (HER) in 0.5 M H₂SO₄.²⁵ The concept has been successfully extended to CoPt,²⁶ CuPt,^{27,28} and ZnPt.²⁹

Similar to Pt, Pd can also alloy with Fe, forming fcc-FePd and fct-FePd.^{30,31} In the core/shell fct-FePd/Pd structure, the tightly packed fct-FePd may cause the Pd shell to “shrink”, stabilizing the shell structure against acid corrosion. Here we demonstrate our studies on the synthesis of core/shell fct-FePd/Pd NPs and their enhanced catalysis for ORR in 0.1 M HClO₄ with Pt-like activity and durability. Figure 1 illustrates the synthesis of core/shell fct-FePd/Pd NPs. First, the Pd NPs are coated with a thin layer of Fe₃O₄, and the core/shell Pd/Fe₃O₄ NPs are annealed in the reducing atmosphere at 600 °C to reduce Fe₃O₄ to Fe and to promote Pd/Fe diffusion into ferromagnetic fct-FePd NPs. The core/shell fct-FePd/Pd NPs are then formed by controlled surface Fe etching from the fct-FePd NPs followed by 400 °C reductive annealing. Here the 400 °C annealing is used to “heal” the Pd shell defects generated from the Fe etching process and to smoothen the Pd shell. The degree of the Fe/Pd ordering in the fct-structure (characterized by magnetic coercivity) is controlled by annealing time at 600 °C, while the Pd shell thickness is tuned from 0.27 to 0.81 nm by Fe-etching temperature. The ORR catalysis of fct-FePd/Pd NPs is dependent both on the degree of the Fe/Pd ordering and on the thickness of the Pd shell. Ferromagnetic fct-FePd/Pd NPs with 0.65 nm thick Pd shell and room-temperature coercivity of 1.0 kOe are the most efficient catalyst for ORR in 0.1 M HClO₄, comparable to the commercial Pt.

RESULTS AND DISCUSSION

To prepare the core/shell fct-FePd/Pd NPs, we first synthesized oleylamine (OAm)-capped Pd NPs by borane morpholine complex reduction of Pd(acac)₂ (acac = acetylacetonate)⁴ and then coated these Pd NPs with Fe₃O₄ via thermal decomposition of Fe(CO)₅ in 1,2,3,4-tetrahydronaphthalene at 180 °C followed by air oxidation. The Fe/Pd composition was controlled by the Fe(CO)₅/Pd molar ratio and analyzed by inductively coupled plasma-atomic emission spectroscopy (ICP-AES) (Figure S1). Figure 2a shows a typical transmission electron microscopy (TEM) image of the Pd/Fe₃O₄ NPs (diameter: 8.5 ± 0.3 nm and the Fe/Pd ratio = 46/54).

We then deposited the Pd/Fe₃O₄ NPs on Ketjen carbon (C) and annealed them at temperatures up to

600 °C in Ar + 4% H₂. In this high-temperature reductive annealing condition, Fe₃O₄ was reduced to Fe, leaving behind defects in the Fe lattice which facilitated Fe–Pd interdiffusion and the formation of fct-FePd NPs, similar to the synthesis of fct-FePt NPs.³² The annealing temperature of 600 °C and Fe/Pd ratio of 46/54 were found to be optimal for the formation of fct-FePd phase. Too much Fe or Pd in the Pd/Fe₃O₄ structure or annealing at temperatures lower than 600 °C led to the formation of fcc-FePd NPs. Figures 2b and S2 give the typical TEM and high resolution TEM (HRTEM) images of the fct-Fe₄₆Pd₅₄ NPs (obtained from annealing at 600 °C for 3 h) on carbon support (denoted as C-fct-FePd), which show an average size of 8.5 ± 0.5 nm and (111) lattice fringe distance of 0.219 nm. The NPs remain well-dispersed on carbon and show no sign of aggregation/sintering after the thermal treatment. Figure 2c is the 2D scanning TEM-electron energy-loss spectroscopy (STEM-EELS) elemental mapping of one representative fct-Fe₄₆Pd₅₄ NP. The mapping shows clearly the Fe diffusion into Pd lattice. The structure and the related magnetic property changes upon Fe–Pd diffusion were monitored by X-ray diffraction (XRD) patterns and vibrating sample magnetometer (VSM) measurements. Compared with the original 8 nm Pd NPs, the fcc-Fe₄₆Pd₅₄ (obtained from annealing at 400 °C for 1 h) and fct-Fe₄₆Pd₅₄ show obvious (111) peak shift to a larger angle (Figure 2d), confirming that the (111) lattice is compressed due to the Fe alloying with Pd. The formation of fct-FePd structure is further evidenced by the appearance of characteristic superlattice peaks (marked by black arrows). The room-temperature VSM measurements show that fcc-Fe₄₆Pd₅₄ NPs are superparamagnetic with their magnetic moment saturated at 169 emu·g^{−1}_{FePd}, while the fct-Fe₄₆Pd₅₄ NPs are ferromagnetic (coercivity H_c = 1.0 kOe) with their moment saturated at 132 emu·g^{−1}_{FePd} (Figure 2e), indicating the strong Fe–Pd interaction in the fct-structure. The degree of Fe/Pd ordering in the Fe₄₆Pd₅₄ structure is related to H_c ; the larger the H_c , the higher the ordering degree. From the annealing-dependent H_c data (Figure 2f) we can see that longer annealing time can help to increase the NP H_c and therefore to increase Fe/Pd ordering. But too long an annealing (over 3 h) can cause the FePd NPs to aggregate/sinter (Figure S3).

To test FePd structure-dependent catalysis, the C-fcc-FePd annealed at 400 °C for 1 h and C-fct-FePd annealed at 600 °C for 1 h (H_c = 0.3 kOe), 2 h (H_c = 0.6 kOe) and 3 h (H_c = 1.0 kOe) were selected for catalytic studies. Figure 3a,b presents their ORR polarization curves and corresponding mass activities, which are then compared to the commercial Pd (denoted as C–Pd) and Pt catalyst (20% mass loading with 2.5–3.5 nm Pt NPs, denoted as C–Pt). All C-FePd catalysts are more active than the C–Pd one with their polarization curves positively shifted, confirming that

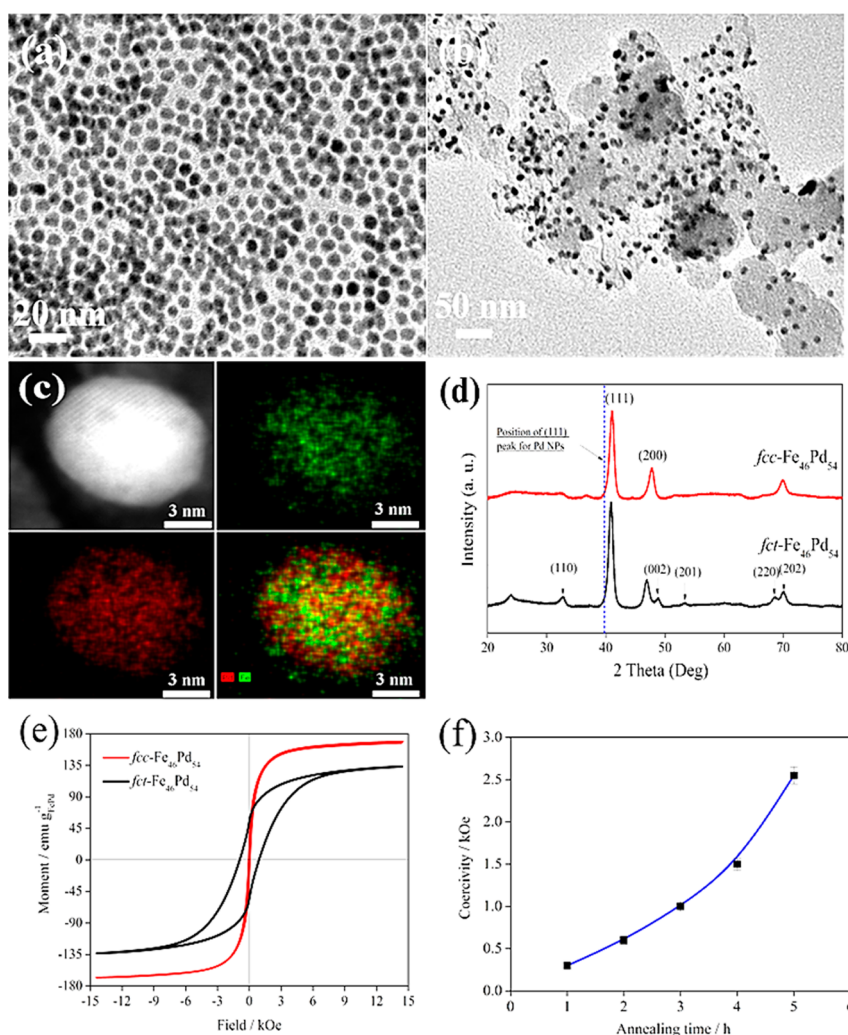


Figure 2. (a) TEM image of the as-synthesized Pd/Fe₃O₄ NPs with the Fe/Pd ratio of 46/54. (b) TEM image of the C-fct-Fe₄₆Pd₅₄ NPs after annealed at 600 °C for 3 h. (c) 2D EELS elemental mapping of Fe (green) and Pd (red) on a single fct-Fe₄₆Pd₅₄ NP, showing a homogeneous solid solution structure. (d) XRD patterns of the fcc-Fe₄₆Pd₅₄ (obtained from annealing at 400 °C for 1 h) and the fct-Fe₄₆Pd₅₄ (obtained from annealing at 600 °C for 3 h); the dash line denotes (111) peak of the 8 nm Pd NPs. (e) Hysteresis loops of the fcc-Fe₄₆Pd₅₄ and fct-Fe₄₆Pd₅₄. (f) Annealing time-dependent H_c of the ferromagnetic fct-Fe₄₆Pd₅₄.

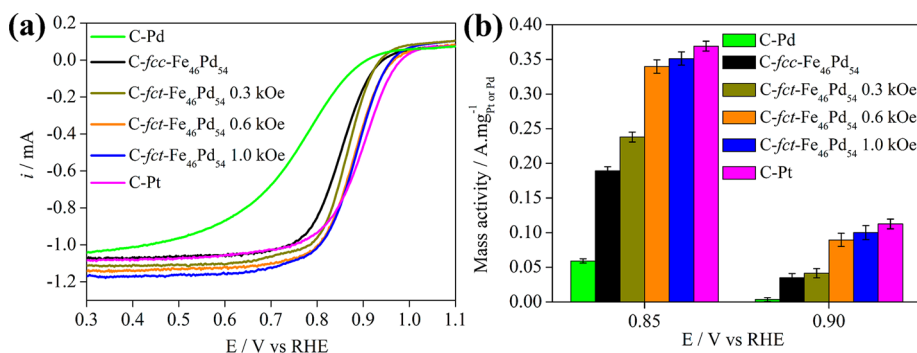


Figure 3. (a) ORR polarization curves and (b) corresponding mass activities of the C-fcc-FePd and C-fct-FePd with different H_c 's, C-Pd, and C-Pt in 0.1 M O₂-saturated HClO₄ solution. The rotating disk electrode was set at a rotation rate of 1600 rpm.

introduction of Fe into Pd lattice enhances the ORR activity. The C-fcc-FePd shows a half-wave potential ($E_{1/2}$) of 0.84 V and mass activities of 34.8 mA·mg⁻¹_{Pd} at 0.90 V and 189 mA·mg⁻¹_{Pd} at 0.85 V, while the C-fct-FePd shows the H_c -dependent increase in $E_{1/2}$'s

(from 0.86 to 0.88 V) and mass activities (from 41.3 to 99.7 mA·mg⁻¹_{Pd} (at 0.90 V) and 238 to 351 mA·mg⁻¹_{Pd} (at 0.85 V). Figure S4a shows the rotation-rate-dependent ORR polarization curves of the C-fct-FePd-1.0 kOe in O₂-saturated HClO₄ solution. From the slopes of the

TABLE 1. Composition Change during the Durability Test of the C-fct-FePd/Pd ($H_c \sim 1.0$ kOe) with Different Pd Shell Thickness

treatment	composition			
	initial	relative standard deviation for Pd ratio	after 3000 cycles	relative standard deviation for Pd ratio
C-fct-FePd-0.27	Fe ₄₄ Pd ₅₆	0.012	Fe ₃₄ Pd ₆₆	0.044
C-fct-FePd-0.65	Fe ₄₁ Pd ₅₉	0.015	Fe ₃₈ Pd ₆₂	0.029
C-fct-FePd-0.81	Fe ₃₇ Pd ₆₃	0.013	Fe ₃₅ Pd ₆₅	0.021

Koutecky–Levich (K-L) equation plots (Figure S4b), we estimated the number of electrons transferred for reducing one oxygen molecule in the ORR to be 3.94–4.02, indicating the ORR on this catalyst proceeds via a 4e process, similar to the case on Pt. The specific activities of these C-FePd catalysts were also found to be H_c dependent (Table S1); the superparamagnetic C-fcc-FePd has the value of $0.051 \text{ mA} \cdot \text{cm}^{-2}$ at 0.90 V, while the ferromagnetic C-fct-FePd's show the increased values from 0.058 (for the catalyst with $H_c = 0.3$ kOe) to $0.168 \text{ mA} \cdot \text{cm}^{-2}$ (for the one with $H_c = 1.0$ kOe) at 0.90 V.

The durability of these catalysts was evaluated by cycling in the potential range of 0.66–1.06 V in 0.1 M O₂-saturated HClO₄ solution, which is characterized by the decay of $E_{1/2}$ after 3000 cycles (Table S2). The C-fcc-FePd has the largest potential decay of ~ 42 mV, while the C-fct-FePd's with the increased H_c become more and more stable with the decay reduced from ~ 40 to ~ 26 mV. These indicate that the higher degree of Fe/Pd ordering in the fct-FePd structure leads not only to larger H_c but also much enhanced ORR catalytic efficiency. The NP morphology (TEM and HRTEM) and Fe/Pd ratios (measured by ICP-AES) of the fcc-FePd, fct-FePd-0.6 kOe, and fct-FePd-1.0 kOe after the durability test were investigated. The HRTEM images in Figure S2 confirm that after the cycling, there is no NP structural change. The fct-FePd NPs with a larger H_c show less NP aggregation (Figure S5) and less Fe loss (fcc-Fe₂₇Pd₇₃ vs fct-Fe₃₂Pd₆₈-1.0 kOe). We can conclude that once the fct-structure is formed, the strong Fe–Pd interaction provides much needed stabilization of the FePd structure and, as a result, enhances both activity and durability of the NP catalyst on ORR.

Although the C-fct-FePd-1.0 kOe shows an enhanced catalysis than its fcc- and less ordered fct-counterparts, it is still not as efficient as the C–Pt catalyst. To further improve the catalytic efficiency, a smooth Pd shell is better formed on the fct-FePd NP surface since such a smooth and compact shell may become more active and the FePd core may be further stabilized.^{33–35} To convert the C-fct-FePd to the core/shell C-fct-FePd/Pd, the alloy NPs were treated in acetic acid at 50 °C overnight to remove the surface Fe. After this treatment, the Fe/Pd ratio was changed from 46/54 to 41/59 (Table 1) and stabilized at this level without further

Fe loss. The product was then annealed in Ar + 4% H₂ at 400 °C for 2 h to form a smooth Pd shell.³³ The TEM image (Figure 4a) shows that the fct-FePd/Pd NPs maintain their original size of 8.5 ± 0.6 nm and morphology after the acid and annealing treatment. To verify whether the fct-structure was preserved during the acid treatment, the hysteresis loops of the C-fct-FePd/Pd were recorded and compared with the C-fct-FePd (Figure S6). The H_c of these two loops is nearly unchanged, indicating the fct-structure preservation within NPs during the treatment. On the other hand, the magnetization value drops after the Pd shell formation, which further confirms the loss of Fe and the formation of Pd shell. The core/shell structure was characterized by the STEM-EELS line scan of a representative single fct-FePd/Pd NP, and the Pd shell thickness was measured to be 0.65 nm, denoted as C-fct-FePd/Pd-0.65 (Figure 4b). HRTEM image in Figure 4c confirms the smooth surface (without 400 °C annealing the Pd shell is defected, Figure S7). The redox properties of the C-fct-FePd/Pd-0.65 before and after 400 °C annealing were studied by cyclic voltammetry. Figure S8 gives their cyclic voltammograms (CVs), showing that the Pd oxide formation and corresponding reduction peak of the annealed C-fct-FePd/Pd-0.65 shifts to a more positive potential compared to the same core/shell NPs without 400 °C treatment. Such a shift is representative of the formation of a smooth Pd shell with less low-coordinated Pd sites after thermal annealing.³⁵ The high-angle annular dark field (HAADF)-STEM image (inset of Figure 4d) and the HAADF line scan profile of the C-fct-FePd/Pd-0.65 NP (Figure 4d) confirm the formation of the Pd shell and the intermetallic FePd core. We should also mention that in the Fe etching experiment, the Pd shell thickness was controlled by the etching temperature. For example, when treated in acetic acid at 25 °C (or 70 °C), the NPs changed their Fe/Pd ratios from 46/54 to 44/56 (or to 37/63), generating a 0.27 (or 0.81 nm) shell, denoted as C-fct-FePd/Pd-0.27 (or C-fct-FePd/Pd-0.81) (Figure S9). In general, acetic acid etching at a higher temperature tends to release more Fe from the fct-FePd, resulting in a thicker Pd shell.

Figure 5a,b compares the ORR polarization curves and corresponding mass activities at 0.90 V for the C-fct-FePd/Pd-0.65 and the commercial Pt catalyst

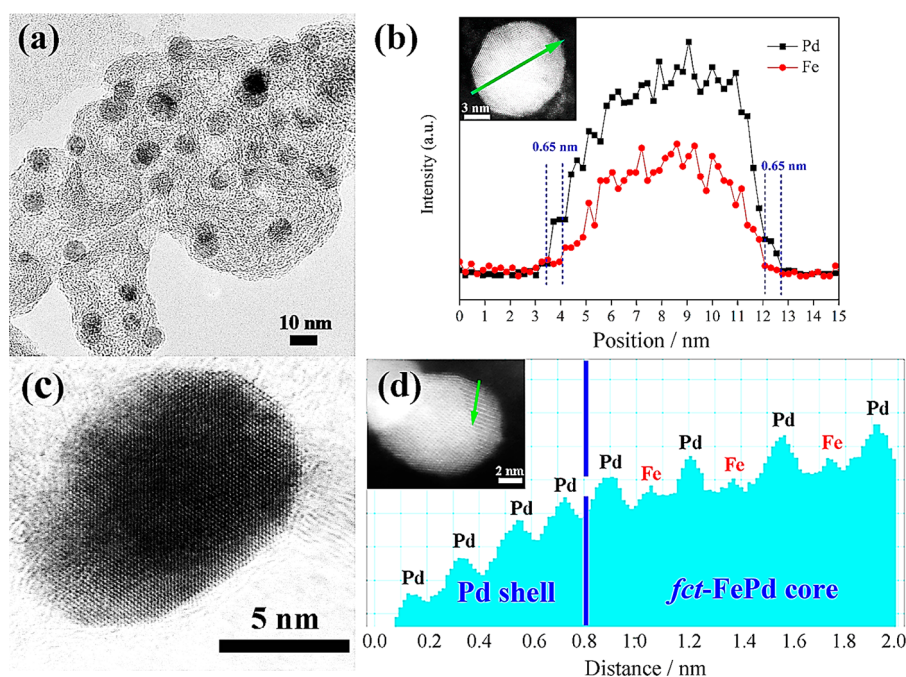


Figure 4. (a) TEM of the C-fct-FePd/Pd-0.65 NPs. (b) STEM-EELS line scan crossing one fct-FePd/Pd-0.65 NP. The inset shows the NP scanned. (c) HRTEM of one fct-FePd/Pd-0.65 NP. (d) HAADF-STEM image of a representative fct-FePd/Pd-0.65 NP with the scan direction from the shell to the core, and the corresponding HAADF line profile normalized with Z contrast of metal atoms; the inset shows the NP scanned.

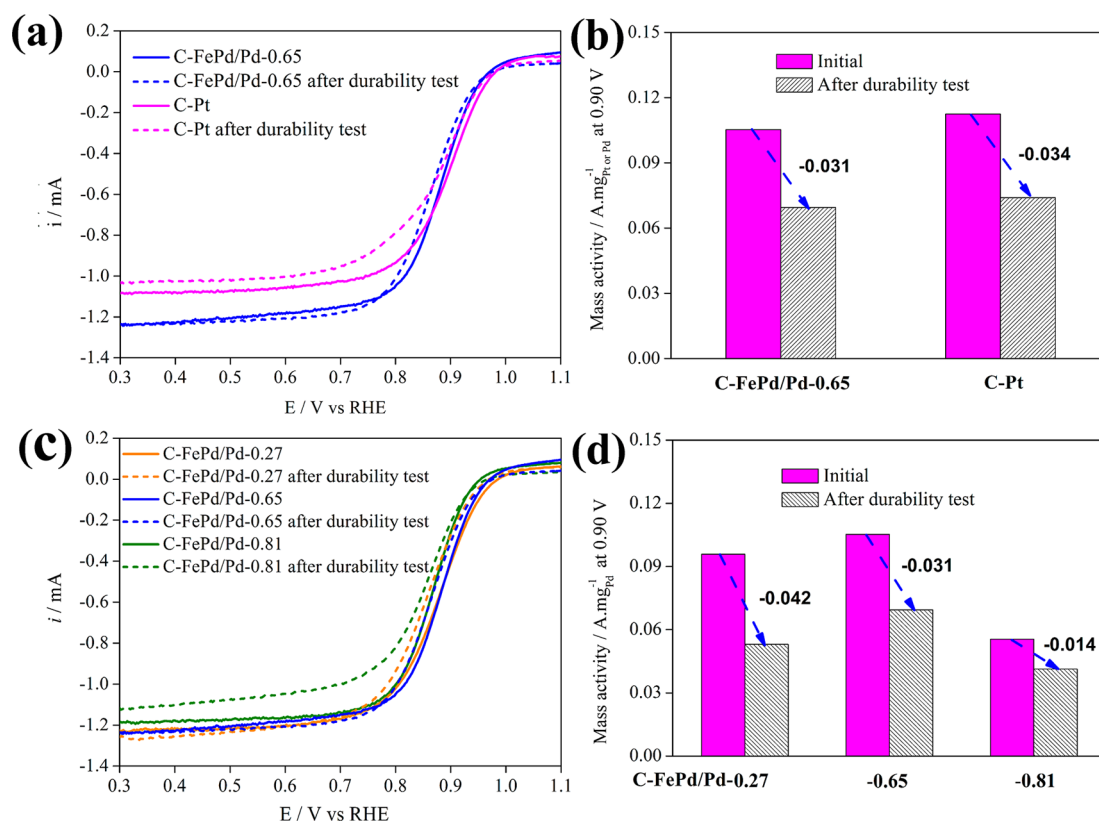


Figure 5. (a) ORR polarization curves and (b) the corresponding mass activities at 0.90 V for the C-fct-FePd/Pd-0.65 and C-Pt before and after durability test in O₂-saturated 0.1 M HClO₄. (c) ORR polarization curves and (d) the corresponding mass activities at 0.90 V for the C-fct-FePd/Pd with different shell thicknesses before and after durability test in O₂-saturated 0.1 M HClO₄.

before and after durability test. The C-fct-FePd/Pd-0.65 has an $E_{1/2}$ of 0.88 V and mass activity of $105 \text{ mA} \cdot \text{mg}^{-1}_{\text{Pd}}$, slightly higher than 0.88 V and $99.7 \text{ mA} \cdot \text{mg}^{-1}_{\text{Pd}}$ for the C-fct-FePd-1.0 kOe and close to 0.89 V and $112 \text{ mA} \cdot \text{mg}^{-1}_{\text{Pt}}$ from the C–Pt. The durability test shows that after 3000 cycles, the C-fct-FePd/Pd-0.65 has an $E_{1/2}$ decay of $\sim 14 \text{ mV}$ and a mass activity drop of $31 \text{ mA} \cdot \text{mg}^{-1}_{\text{Pd}}$, better than the C-fct-FePd ($\sim 26 \text{ mV}$ decay), indicating that the smooth Pd shell significantly improves the catalyst durability, which is even comparable to the C–Pt with $\sim 15 \text{ mV}$ decay and mass activity drop of $34 \text{ mA} \cdot \text{mg}^{-1}_{\text{Pt}}$. Figure S5e shows the TEM image of the C-fct-FePd/Pd-0.65 after the durability test, showing no obvious NP aggregation. These suggest that the fct-FePd/Pd with the smooth 0.65 nm Pd shell can perform comparably to the C–Pt on ORR catalysis.

Studies on Pd-shell thickness dependent ORR catalysis for the C-fct-FePd/Pd NPs (Figure 5c,d and Table S1) show that the C-fct-FePd/Pd-0.81 is much less active, and its mass activity and specific activity at 0.90 V are only near 1/2 and 2/3 of those for the C-fct-FePd/Pd-0.65, respectively, implying that an overthick Pd shell deactivates the core/shell catalyst. In the durability test, the C-fct-FePd/Pd-0.81 had a negative $E_{1/2}$ shift of $\sim 11 \text{ mV}$ and a mass activity drop of $14 \text{ mA} \cdot \text{mg}^{-1}_{\text{Pd}}$, better than the C-fct-FePd/Pd-0.65 ($\sim 14 \text{ mV}$ and $31 \text{ mA} \cdot \text{mg}^{-1}_{\text{Pd}}$) and the C-fct-FePd/Pd-0.27 ($\sim 23 \text{ mV}$ and $42 \text{ mA} \cdot \text{mg}^{-1}_{\text{Pd}}$). Figure S5d–f shows the TEM images of these C-fct-FePd/Pd catalysts after the cycling. All the C-fct-FePd/Pd show less NP aggregation compared to the C-fct-FePd, suggesting that the smooth Pd shell helps stabilize the NP. Fe/Pd ratios in the C-fct-FePd/PdNPs before and after the durability tests were analyzed by ICP-AES. The C-fct-FePd/Pd-0.81 and C-fct-FePd/Pd-0.65 NPs lost only 2–3% Fe, while the C-fct-FePd/Pd-0.27 NPs had a 10% Fe reduction (Table 1), suggesting 0.27 nm Pd shell is too thin to protect Fe from leaching from the core. Overall, among three different C-fct-FePd/Pd tested, the C-fct-FePd/Pd-0.65 NPs are the best catalyst for ORR with Pt-like activity and durability.

To understand why the core/shell C-fct-FePd/Pd NPs show the shell thickness dependent ORR activity, we performed theoretical simulation on this system. In general, both surface strain and ligand effect could influence catalytic activities of core/shell NPs. However, it has been shown that the ligand effect is often negligible for core/shell NPs with a thickness $> 0.6 \text{ nm}$.³⁶ Therefore, we focus on the surface strain to elucidate the superior ORR activity on NPs with 0.65 nm shell to those with 0.81 nm shell. To this end, we calculated oxygen adsorption energy (E_{O}), which is an excellent descriptor for ORR activity. There exists an optimal E_{O} value under which the ORR activity of the catalyst reaches the maximum.^{37,38} In convenience, we set the optimal E_{O} at 0 eV, and ΔE_{O} is defined relative to

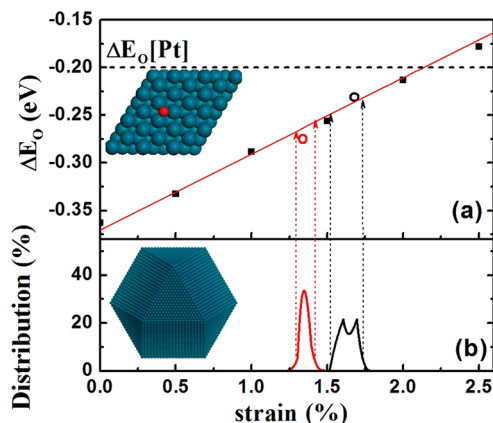


Figure 6. (a) ΔE_{O} as a function of compressive strain on Pd (111) surface. The red line is a linear fit to the DFT values of ΔE_{O} . The optimal E_{O} value is set to be zero. Black and red circle represents ΔE_{O} for fct-FePd/Pd-0.6 NP and fct-FePd/Pd-0.8 NP, respectively, obtained from the QM-MM calculations. (b) The percentage distribution of surface strain on the (111) facets of fct-FePd/Pd-0.6 NP (black) and fct-FePd/Pd-0.8 NP (red).

this optimal value. Both density functional theory (DFT) and quantum mechanics-molecular mechanics (QM-MM) calculations were performed to determine ΔE_{O} . First, a flat Pd (111) surface is modeled under a lateral compression up to 2.5% with DFT as shown in Figure 6a. The DFT calculations reveal a linear relationship between the surface strain and ΔE_{O} . A more compressive strain would shift E_{O} toward the value on the Pt (111). In particular, the Pd surface with a compressive strain of $\sim 2.1\%$ could yield the same ORR activity as the Pt surface. We then modeled an 8 nm fct-FePd/Pd NP with 0.6 nm Pd shell thickness. The lattice mismatch between the fct-FePd core and the Pd-shell generates $\sim 1.7\%$ compressive strain on the NP surface; the corresponding ΔE_{O} value is -0.25 eV , which is close to the value (-0.2 eV) on Pt (111). Hence the ORR activity on the fct-FePd/Pd-0.6 NP should approach that on Pt. As the shell thickness increases to 0.8 nm, the compressive surface strain is released as indicated in Figure 6b. ΔE_{O} becomes more negative leading to a less active ORR catalysis. Therefore, the superior ORR activity of fct-FePd/Pd-0.6 NPs stems from the desired compressive strain. Note that a thicker NP could release its stress more readily than a thinner one. Hence the strain distribution on the 0.8 nm NPs is more uniform (or less broadened) than that on the thinner one (0.6 nm), as shown in Figure 6b.

For NPs with 0.2 nm shell, the ligand effect cannot be ignored. Here we calculate ΔE_{O} on a monolayer Pd (0.2 nm interlayer distance), which is deposited on a flat fct-FePd surface. The ΔE_{O} value becomes positive (0.29 eV) and moves to the other side of the volcano plot.³⁷ The significantly weakened Pd–O binding is due to the ligand effect. As the ΔE_{O} value of the 0.2 nm shell is farther away from the optimal value than that of 0.6 nm shell, the corresponding core/shell NPs with the

0.2 nm shell cannot exhibit higher ORR activities, consistent with our experimental observations.

CONCLUSION

In conclusion, we have synthesized fcc-FePd and fct-FePd *via* reductive annealing of core/shell Pd/Fe₃O₄ NPs. The degree of the Fe/Pd ordering in the fct-FePd (characterized by the increase of magnetic coercivity from 0.3 to 2.55 kOe) can be controlled by the thermal annealing. The stronger ferromagnetic fct-FePd shows higher ORR activity and durability in 0.1 M HClO₄ than the fcc-FePd. When etched with acetic acid at a controlled temperature (from 25 to 70 °C), the fct-FePd NPs

are converted to core/shell fct-FePd/Pd NPs with the Pd shell thickness controlled to be 0.27, 0.65, or 0.81 nm. The 1.0 kOe fct-FePd/Pd NPs with 0.65 nm Pd shell are more active and durable for ORR than any other FePd NPs studied here, and they even show the Pt-like activity and durability. By examining both the strain and ligand effects, our DFT simulations suggest that the high ORR activity originates from the desired compressive strain on the 0.65 nm Pd shell induced by the fct-FePd core. Our result demonstrates a new way of tuning Pd catalysis for ORR. It will help to develop Pd-based NPs as a new class of non-Pt catalyst for ORR and other chemical reactions in acid media.

METHODS

Materials. Oleylamine (OAm, >70%), 1,2,3,4-tetrahydronaphthalene, Pd(acac)₂ (acac = acetylacetonate), borane morpholine complex, Fe(CO)₅, acetic acid, hexane, isopropanol, ethanol, and Nafion (5%) were all purchased from Sigma-Aldrich.

Synthesis of Pd NPs. Pd NPs were prepared following the reported method.⁴ In a reaction flask with a continuous N₂ flow and magnetic stirring, 0.5 mmol of Pd(acac)₂ was dissolved in 15 mL of OAm, and the solution was heated to 40 °C. After 30 min of heating at 40 °C, 2.5 mmol of borane morpholine complex predissolved in 4 mL of OAm was injected into the solution, leading to an instant color change from transparent yellow to black-brown. The solution was then heated to 90 °C at a rate of 3 °C/min and kept at this temperature for 1 h. Once cooled down to room temperature, the Pd NPs were collected by adding ethanol and centrifugation. The NPs were further purified with hexane/ethanol and redispersed in hexane for further use.

Synthesis of Pd/Fe₃O₄ NPs. A solution of 0.20 mmol of Pd NPs in 3 mL hexane was mixed with 12 mL 1,2,3,4-tetrahydronaphthalene and 0.34 mL OAm. The solution was heated to 40 °C under a continuous N₂ flow to remove hexane. After 30 min, the temperature was raised to 120 °C, and under a blanket of N₂ protection, a controlled amount of Fe(CO)₅ was injected into the solution to initiate Fe nucleation on the Pd seeds. The solution was further heated to 180 °C at a rate of 3–4 °C/min and kept at this temperature for 30 min before cooled down to room temperature. The reaction system was then open to air, and Pd/Fe₃O₄ NPs were obtained and collected by adding isopropanol and centrifugation. The NPs were further purified with hexane/ethanol and stored in hexane. The relationship between the amount of Fe(CO)₅ added and final Pd content in the Pd/Fe₃O₄ NPs is shown in Figure S1.

Catalyst Preparation. The as-synthesized Pd/Fe₃O₄ NPs and Ketjen-300J carbon at a mass ratio of 1:2 were mixed in 20 mL hexane and sonicated for 1 h to deposit NPs on the carbon (C–Pd/Fe₃O₄). The C–Pd/Fe₃O₄ was separated by centrifugation (8500 rpm, 3 min) and then dried under ambient conditions. The collected NP powder was annealed at different temperatures (400 and 600 °C) in a gas flow of Ar + 4% H₂ to generate fcc-FePd and fct-FePd NPs. The annealing time varied from 1 to 5 h to control the degree of fcc- to fct-phase transition. After annealing, the C-NPs were mixed with 25 mL acetic acid and stirred magnetically under a gentle N₂ flow overnight to remove surface Fe. Different temperatures of 25, 50, and 70 °C were used to control the etching degree of surface Fe. The product was washed with deionized water and ethanol twice to remove the excess acetic acid and dried in ambient conditions to form black powders. The treated samples were then annealed at 400 °C for 2 h under a gentle Ar + 4% H₂ flow to form a smooth Pd shell on the NP surface.

Electrochemical Measurements. The catalyst was suspended in a mixture of deionized water, isopropanol, and Nafion

(V/V/V = 4/1/0.05) to form an ink. Twenty μ L ink (2 mg/mL) was deposited on the polished glassy carbon (GC) working electrode and dried in ambient conditions. The catalyst was first cycled at 100 mV/s in 0.1 M HClO₄ until stable CVs were obtained. Linear scan voltammetry was conducted in an O₂-saturated 0.1 M HClO₄ solution by sweeping the potential from 0.26 to 1.06 V vs reversible hydrogen electrode (RHE) at a scan rate of 10 mV/s and electrode rotation of 1600 rpm. The durability test was conducted by cycling the potentials between 0.66 and 1.06 V vs RHE at a rate of 100 mV/s for 3000 cycles in O₂-saturated 0.1 M HClO₄. Mass and specific activities were obtained at 0.90 and 0.85 V and depicted as kinetic current densities normalized to Pd or Pt mass loading and to the electrochemical active surface area (ECASA). Here, the Pt and Pd loading were analyzed by the ICP-AES. The ECASA of Pd-based catalysts were obtained by integrating the reduction peaks of Pd oxide in their CVs.

Characterization. TEM images were obtained from a Philips CM 20 operated at 200 kV. HRTEM images were acquired on a JEOL 2100F (200 kV). Each sample was prepared by depositing a single drop of diluted NPs dispersion on an amorphous carbon-coated copper grid. STEM analyses were carried out on FEI Titan G2 80–200 (200 kV) with a Cs-corrector at Zhejiang University. The EELS line-scan was obtained by a high-resolution Gatan-Enfina ER with a probe size of 0.8 Å. A power law function was used for EELS background subtraction. To determine the Fe/Pd ratio, the catalyst was first digested with aqua regia (HNO₃/HCl = 1/3 in volume) at 200 °C and then diluted by 2% HNO₃ aqueous solution. The solution was then filtrated to remove the residue carbon, and the filtrate were collected for ICP-AES measurements, which were carried on a JY2000 Ultracore ICP atomic emission spectrometer equipped with a JY A5 421 autosampler and 2400 g/mm holographic grating. X-ray diffraction (XRD) characterization was carried out on a Bruker AXS D8-Advanced diffractometer with Cu K α radiation (λ = 1.5418 Å). Electrochemical measurements were carried out on an Autolab potentiostat from Metrohm Instrument Company (Autolab 302). A three-electrode system consisting of a GC working electrode (5 mm in diameter), a Ag/AgCl reference electrode (in saturated KCl), and a platinum wire counter electrode was used for electrochemical studies. All the potentials were calibrated vs RHE.

DFT Calculation of ΔE_O on Pd Surface. The E_O value was determined by placing an O atom on the fcc hollow site of (111) surface, following

$$E_O = E_{[\text{Pd}+\text{O}]} - E_{[\text{Pd}]} - E_{[\text{O}_2]}/2$$

where $E_{[\text{Pd}+\text{O}]}$ and $E_{[\text{Pd}]}$ are total energies of the Pd surface with and without O adsorbate, respectively. $E_{[\text{O}_2]}$ is the total energy of a oxygen molecule. For DFT calculations of Pd surface, we used $3 \times 3 \times (\sqrt{3} \times \sqrt{3})\text{R}30^\circ$ unit cells. A four-layer slab was used for these calculations with the top two layers fully relaxed. For the slab of fct-FePd/Pd, the first top layer is pure Pd, and the remaining three layers consist of fct-FePd. The ΔE_O value was

then calculated by shifting E_O relative to the optimal value. The DFT calculations were carried out using the VASP package^{39,40} with the projector augmented wave pseudopotentials (PAW)⁴¹ and Perdew–Burke–Ernzerhof generalized gradient approximation (PBE-GGA).⁴² An energy cutoff of 400 eV was used for the plane-wave basis set. The Brillouin zone was sampled on the basis of the Monkhorst–Pack scheme⁴³ with a $3 \times 3 \times 1$ k -point mesh. The force convergence criterion for atomic relaxation is 0.02 eV/Å. For systems with presence of Fe, spin-polarized calculations are performed.

Computational Models of the Core/Shell NPs. The fct-FePd/Pd NPs are modeled by 8 nm cuboctahedrons with eight (111) facets and six (100) facets as shown in Figure 6b. The NP consists of a fcc-Pd shell and a fct-FePd core. To study the shell thickness effects on ORR, we have considered two core/shell NPs with shell thickness of 0.6 and 0.8 nm denoted as fct-FePd/Pd-0.6 NP and fct-FePd/Pd-0.8 NP, respectively. Note that these shell thicknesses are slightly different from the experimental values. The minor differences (~ 0.05 nm) reflect the precision of the experimental measurements. Since the ORR activity is influenced by the lateral strain as opposed to the vertical strain, these differences are inconsequential.

Calculation of Surface Strains on NPs. All atoms of the core/shell NPs were fully relaxed by the embedded atom method with interatomic potentials.⁴⁴ There are eight (111) facets in the cuboctahedral NP, and for each (111) facet we selected 37 O adsorbed sites (fcc hollow sites) to measure the local strain. Thus, for each NP model, 296 sites were included in the strain distribution.

QM-MM Simulations. As shown in Figure S10, the entire NP model is partitioned into two spatial domains: a QM region (red, pink and green spheres) treated by DFT and a MM region (blue spheres) by empirical atomistic simulations. The QM region is further divided into an interior QM region (red and pink spheres) and a boundary QM region (green spheres). The technical details and validations of the QM-MM method can be found elsewhere.⁴⁵ The QM region measures $16.9 \times 16.9 \times 8$ Å in x , y , and z directions, respectively with 200 atoms, where the innermost $8.3 \times 7.2 \times 4$ Å is the interior QM region containing the adsorbed oxygen atom on the fcc hollow site. The MM region consists of the rest of the system where the strain effect due to the core/shell lattice mismatch can be captured. The DFT calculations are carried out using the VASP package with the PAW and PBE-GGA. The calculations are performed at Γ point with 400 eV energy cutoff. The EAM potentials⁴⁴ are used in the MM simulations, which have been rescaled to yield the same lattice constant and bulk modulus as those of DFT. The force convergence criterion for atomic relaxation is 0.03 eV/Å. The E_O value was determined by placing an O atom on the fcc hollow site at the center of the (111) facet, following

$$E_O = \text{EQM-MM}_{[\text{NP}+\text{O}]} - \text{EQM-MM}_{[\text{NP}]} - E_{[\text{O}2]}/2$$

where $\text{EQM-MM}_{[\text{NP}+\text{O}]}$ and $\text{EQM-MM}_{[\text{NP}]}$ are total energies of the core/shell NP with and without O adsorbate, respectively, from QM-MM calculations. And the local strain value is measured at the center of the (111) facet within the interior QM region.

Conflict of Interest: The authors declare no competing financial interest.

Supporting Information Available: The Supporting Information is available free of charge on the ACS Publications website at DOI: 10.1021/acsnano.5b04361.

Relationship between the amount of $\text{Fe}(\text{CO})_5$ and the Pd content within Pd/ Fe_3O_4 NPs; HRTEM images of the C-fct-FePd and C-fcc-FePd NPs before and after cycling; TEM images of C-FePd after annealing; ORR polarization curves for C-fct-FePd at different rotation rates and corresponding K-L plots; TEM images of the C-FePd after cycling; Hysteresis loops of the fct-FePd and corresponding fct-FePd/Pd; HRTEM image of single representative fct-FePd/Pd NP; CVs of the C-fct-FePd/Pd-0.65 before and after thermal annealing; STEM-EELS line scan crossing one fct-FePd/Pd NP after acetic acid treatment; Atomic configuration of a cuboctahedral NP for QM-MM calculation (PDF)

Acknowledgment. This work was supported by U.S. Army Research Laboratory and the U.S. Army Research Office under the Multi University Research Initiative (MURI, grant number W911NF-11-1-0353) on “Stress-Controlled Catalysis via Engineered Nanostructures” and National Natural Science Foundation of China (Project 51508055).

REFERENCES AND NOTES

- Bianchini, C.; Shen, P. K. Palladium-based Electrocatalysts for Alcohol Oxidation in Half Cells and in Direct Alcohol Fuel Cells. *Chem. Rev.* **2009**, *109*, 4183–4206.
- Zhang, H.; Jin, M.; Xiong, Y.; Lim, B.; Xia, Y. Shape-Controlled Synthesis of Pd Nanocrystals and Their Catalytic Applications. *Acc. Chem. Res.* **2013**, *46*, 1783–1794.
- Chang, J. F.; Feng, L. G.; Liu, C. P.; Xing, W.; Hu, X. L. An Effective Pd-Ni₂P/C Anode Catalyst for Direct Formic Acid Fuel Cells. *Angew. Chem., Int. Ed.* **2014**, *53*, 122–126.
- Mazumder, V.; Sun, S. Oleamine-Mediated Synthesis of Pd Nanoparticles for Catalytic Formic Acid Oxidation. *J. Am. Chem. Soc.* **2009**, *131*, 4588–4589.
- Jin, M.; Zhang, H.; Xie, Z.; Xia, Y. Palladium Concave Nanocubes with High-Index Facets and Their Enhanced Catalytic Properties. *Angew. Chem., Int. Ed.* **2011**, *50*, 7850–7854.
- Shao, M.; He, G.; Peles, A.; Odell, J. H.; Zeng, J.; Su, D.; Tao, J.; Yu, T.; Zhu, Y.; Xia, Y. Manipulating the Oxygen Reduction Activity of Platinum Shells with Shape-controlled Palladium Nanocrystal Cores. *Chem. Commun.* **2013**, *49*, 9030–9032.
- Xiao, L.; Zhuang, L.; Liu, Y.; Lu, J.; Abruna, H. D. Activating Pd by Morphology Tailoring for Oxygen Reduction. *J. Am. Chem. Soc.* **2009**, *131*, 602–608.
- Zheng, Y.; Zhao, S.; Liu, S.; Yin, H.; Chen, Y. Y.; Bao, J.; Han, M.; Dai, Z. Component-Controlled Synthesis and Assembly of Cu-Pd Nanocrystals on Graphene for Oxygen Reduction Reaction. *ACS Appl. Mater. Interfaces* **2015**, *7*, 5347–5357.
- Gong, K.; Du, F.; Xia, Z.; Durstock, M.; Dai, L. Nitrogen-Doped Carbon Nanotube Arrays with High Electrocatalytic Activity for Oxygen Reduction. *Science* **2009**, *323*, 760–764.
- Zitolo, A.; Goellner, V.; Armel, V.; Sougrati, M. T.; Mineva, T.; Stievano, L.; Fonda, E.; Jaouen, F. Identification of Catalytic Sites for Oxygen Reduction in Iron- and Nitrogen-Doped Graphene Materials. *Nat. Mater.* **2015**, *14*, 937–942.
- Liang, Y.; Li, Y.; Wang, H.; Zhou, J.; Wang, J.; Regier, T.; Dai, H. Co₃O₄ Nanocrystals on Graphene as a Synergistic Catalyst for Oxygen Reduction Reaction. *Nat. Mater.* **2011**, *10*, 780–786.
- Holewinski, A.; Idrobo, J. C.; Linic, S. High-performance Ag-Co Alloy Catalysts for Electrochemical Oxygen Reduction. *Nat. Chem.* **2014**, *6*, 828–834.
- Mazumder, V.; Chi, M.; Mankin, M. N.; Liu, Y.; Metin, O.; Sun, D.; More, K. L.; Sun, S. A Facile Synthesis of MPd (M = Co, Cu) Nanoparticles and Their Catalysis for Formic Acid Oxidation. *Nano Lett.* **2012**, *12*, 1102–1106.
- Liu, S.; Zhang, Q.; Li, Y.; Han, M.; Gu, L.; Nan, C.; Bao, J.; Dai, Z. Five-Fold Twinned Pd₂NiAg Nanocrystals with Increased Surface Ni Site Availability to Improve Oxygen Reduction Activity. *J. Am. Chem. Soc.* **2015**, *137*, 2820–2823.
- Suo, Y.; Zhuang, L.; Lu, J. First-principles Considerations in the Design of Pd-Alloy Catalysts for Oxygen Reduction. *Angew. Chem., Int. Ed.* **2007**, *46*, 2862–2864.
- Shao, M. H.; Sasaki, K.; Adzic, R. R. Pd-Fe Nanoparticles as Electrocatalysts for Oxygen Reduction. *J. Am. Chem. Soc.* **2006**, *128*, 3526–3527.
- Shao, M. H.; Huang, T.; Liu, P.; Zhang, J.; Sasaki, K.; Vukmircovic, M. B.; Adzic, R. R. Palladium Monolayer and Palladium Alloy Electrocatalysts for Oxygen Reduction. *Langmuir* **2006**, *22*, 10409–10415.
- Shao, M.; Liu, P.; Zhang, J.; Adzic, R. R. Origin of Enhanced Activity in Palladium Alloy Electrocatalysts for Oxygen Reduction Reaction. *J. Phys. Chem. B* **2007**, *111*, 6772–6775.
- Wang, D.; Xin, H. L.; Yu, Y.; Wang, H.; Rus, E.; Muller, D. A.; Abruna, H. D. Pt-decorated PdCo@Pd/C Core-Shell Nanoparticles with Enhanced Stability and Electrocatalytic

- Activity for the Oxygen Reduction Reaction. *J. Am. Chem. Soc.* **2010**, *132*, 17664–17666.
20. Fernandez, J. L.; Raghuvver, V.; Manthiram, A.; Bard, A. J. Pd-Ti and Pd-Co-Au Electrocatalysts as a Replacement for Platinum for Oxygen Reduction in Proton Exchange Membrane Fuel Cells. *J. Am. Chem. Soc.* **2005**, *127*, 13100–13101.
 21. Antolini, E. Effect of Structural Characteristics of Binary Palladium-Cobalt Fuel Cell Catalysts on the Activity for Oxygen Reduction. *ChemPlusChem* **2014**, *79*, 765–775.
 22. Kim, J.; Lee, Y.; Sun, S. Structurally Ordered FePt Nanoparticles and Their Enhanced Catalysis for Oxygen Reduction Reaction. *J. Am. Chem. Soc.* **2010**, *132*, 4996–4997.
 23. Kim, J.; Rong, C.; Liu, J. P.; Sun, S. Dispersible Ferromagnetic FePt Nanoparticles. *Adv. Mater.* **2009**, *21*, 906–909.
 24. Zhang, S.; Zhang, X.; Jiang, G.; Zhu, H.; Guo, S.; Su, D.; Lu, G.; Sun, S. Tuning Nanoparticle Structure and Surface Strain for Catalysis Optimization. *J. Am. Chem. Soc.* **2014**, *136*, 7734–7739.
 25. Li, Q.; Wu, L.; Wu, G.; Su, D.; Lv, H.; Zhang, S.; Zhu, W.; Casimir, A.; Zhu, H.; Mendoza-Garcia, A.; et al. New Approach to Fully Ordered fct-FePt Nanoparticles for Much Enhanced Electrocatalysis in Acid. *Nano Lett.* **2015**, *15*, 2468–2473.
 26. Wang, D.; Xin, H.; Hovden, R.; Wang, H.; Yu, Y.; Muller, D. A.; DiSalvo, F. J.; Abruna, H. D. Structurally Ordered Intermetallic Platinum-Cobalt Core-Shell Nanoparticles with Enhanced Activity and Stability as Oxygen Reduction Electrocatalysts. *Nat. Mater.* **2013**, *12*, 81–87.
 27. Ghosh, T.; Leonard, B. M.; Zhou, Q.; DiSalvo, F. J. Pt Alloy and Intermetallic Phases with V, Cr, Mn, Ni, and Cu: Synthesis As Nanomaterials and Possible Applications As Fuel Cell Catalysts. *Chem. Mater.* **2010**, *22*, 2190–2202.
 28. Wang, D.; Yu, Y.; Xin, H.; Hovden, R.; Ercius, P.; Mundy, J. A.; Chen, H.; Richard, J. H.; Muller, D. A.; DiSalvo, F. J.; et al. Tuning Oxygen Reduction Reaction Activity via Controllable Dealloying: a Model Study of Ordered Cu₃Pt/C Intermetallic Nanocatalysts. *Nano Lett.* **2012**, *12*, 5230–5238.
 29. Kang, Y.; Pyo, J. B.; Ye, X.; Gordon, T. R.; Murray, C. B. Synthesis, Shape Control, and Methanol Electro-oxidation Properties of Pt-Zn Alloy and Pt₃Zn Intermetallic Nanocrystals. *ACS Nano* **2012**, *6*, 5642–5647.
 30. Yu, Y.; Sun, K.; Tian, Y.; Li, X.; Kramer, M. J.; Sellmyer, D. J.; Shield, J. E.; Sun, S. One-Pot Synthesis of Urchin-like FePd-Fe₃O₄ and Their Conversion into Exchange-Coupled L1₀-FePd-Fe Nanocomposite Magnets. *Nano Lett.* **2013**, *13*, 4975–4979.
 31. Kirkeminde, A.; Ren, S. Interdiffusion Induced Exchange Coupling of L1₀-FePd/alpha-Fe magnetic nanocomposites. *Nano Lett.* **2014**, *14*, 4493–4498.
 32. Liu, F.; Zhu, J.; Yang, W.; Dong, Y.; Hou, Y.; Zhang, C.; Yin, H.; Sun, S. Building Nanocomposite Magnets by Coating a Hard Magnetic Core with a Soft Magnetic Shell. *Angew. Chem., Int. Ed.* **2014**, *53*, 2176–2180.
 33. Zhu, H.; Zhang, S.; Su, D.; Jiang, G.; Sun, S. Surface Profile Control of FeNiPt/Pt Core/Shell Nanowires for Oxygen Reduction Reaction. *Small* **2015**, *11*, 3545–3549.
 34. Zhang, S.; Hao, Y.; Su, D.; Doan-Nguyen, V. V. T.; Wu, Y.; Li, J.; Sun, S.; Murray, C. B. Monodisperse Core/Shell Ni/FePt Nanoparticles and Their Conversion to Ni/Pt to Catalyze Oxygen Reduction. *J. Am. Chem. Soc.* **2014**, *136*, 15921–15924.
 35. Wang, C.; Chi, M.; Li, D.; Strmcnik, D.; van der Vliet, D.; Wang, G.; Komanicky, V.; Chang, K. C.; Paulikas, A. P.; Tripkovic, D.; et al. Design and Synthesis of Bimetallic Electrocatalyst with Multilayered Pt-Skin Surfaces. *J. Am. Chem. Soc.* **2011**, *133*, 14396–14403.
 36. Zhang, X.; Lu, G. Computational Design of Core/Shell Nanoparticles for Oxygen Reduction Reactions. *J. Phys. Chem. Lett.* **2014**, *5*, 292–297.
 37. Nørskov, J. K.; Rossmeisl, J.; Logadottir, A.; Lindqvist, L.; Kitchin, J. R.; Bligaard, T.; Jonsson, H. Origin of the Overpotential for Oxygen Reduction at a Fuel-cell Cathode. *J. Phys. Chem. B* **2004**, *108*, 17886–17892.
 38. Stamenkovic, V.; Mun, B. S.; Mayrhofer, K. J.; Ross, P. N.; Markovic, N. M.; Rossmeisl, J.; Greeley, J.; Nørskov, J. K. Changing the Activity of Electrocatalysts for Oxygen Reduction by Tuning the Surface Electronic Structure. *Angew. Chem., Int. Ed.* **2006**, *45*, 2897–2901.
 39. Kresse, G.; Hafner, J. *Ab initio* Molecular Dynamics for Liquid Metals. *Phys. Rev. B: Condens. Matter Mater. Phys.* **1993**, *47*, 558–561.
 40. Kresse, G.; Furthmüller, J. Efficient Iterative Schemes for *abinitio* Total-energy Calculations Using a Plane-wave Basis Set. *Phys. Rev. B: Condens. Matter Mater. Phys.* **1996**, *54*, 11169–11186.
 41. Blochl, P. E. Projector Augmented-wave Method. *Phys. Rev. B: Condens. Matter Mater. Phys.* **1994**, *50*, 17953–17979.
 42. Perdew, J. P.; Burke, K.; Ernzerhof, M. Generalized Gradient Approximation Made Simple. *Phys. Rev. Lett.* **1996**, *77*, 3865–3868.
 43. Monkhorst, H. J.; Pack, J. D. Special Points for Brillouin-zone Integrations. *Phys. Rev. B* **1976**, *13*, 5188–5192.
 44. Zhou, X. W.; Johnson, R. A.; Wadley, H. N. G. Misfit-Energy-Increasing Dislocations in Vapor-Deposited CoFe/NiFe-Multilayers. *Phys. Rev. B: Condens. Matter Mater. Phys.* **2004**, *69*, 144113–144122.
 45. Zhang, X.; Lu, G.; Curtin, W. A. Multiscale Quantum/Atomistic Coupling Using Constrained Density Functional Theory. *Phys. Rev. B: Condens. Matter Mater. Phys.* **2013**, *87*, 054113–054122.